Modelling the stochastic dynamic behaviour of a pontoon bridge: a case study

Knut Andreas Kvåle[a], Ragnar Sigbjörnsson[a], Ole Øiseth[a,*]

[a]*Norwegian University of Science and Technology, Trondheim, Norway*

Abstract

Herein, a study on the hydrodynamic modelling of pontoon bridges is presented, with the Bergsøysund Bridge as a representative example. The model relies on the finite element method and linearized potential theory. The primary emphasis is placed on the stochastic response analysis within the framework of the power spectral density method. The quadratic eigenvalue problem is solved using a state-space representation and an iterative algorithm. The contribution of the fluid-structure interaction to the overall modal damping is investigated. Response effects due to changes in the sea state are studied. A frequency-independent approximation of the hydrodynamic coefficients is presented and discussed.

Keywords: Floating bridge, The Bergsøysund Bridge, Stochastic dynamics

1. Introduction

Although the history of floating bridges may be traced back as far as 2000 BC [1], only in recent decades have floating bridges begun to be developed to a sufficient degree of sophistication such that they can be applied as critical components of modern infrastructure. Compared with land-based bridges, including cable-stayed bridges, only limited information on floating bridges is currently available, particularly regarding construction records, environmental conditions, durability, operations and performance. This is clear from the fact that only approximately twenty long floating bridges currently exist throughout the world. The major trends in the development of floating bridges and other very large floating structures (commonly abbreviated VLFSs) have been presented by Wang et al. [2] and Wang and Wang [3].

The state-of-the-art design philosophy for floating bridges in 1997 was outlined by Moe [4]. It was remarked that standard engineering practices were not directly applicable to floating bridges. A verified design code for floating bridge design would drastically reduce the effort required during the planning stage and would thus increase the potential economic advantages of floating bridges over many alternative bridge concepts. From a broader perspective, a unifying, efficient, and reliable method for simulating the behaviour of floating bridges is the primary goal.

The Norwegian Public Roads Administration (NPRA) is currently investigating possible technological solutions for a ferry-free Coastal Highway Route E39 along the western coast of Norway. This route stretches 1100 km between the cities of Kristiansand and Trondheim and requires multiple crossings of deep and wide fjords. The ferry-free crossings of these deep fjords represent considerable engineering challenges that are difficult or impossible to solve using existing bridge technology; pontoon-type floating bridges have been proposed as feasible options.

Of all existing floating bridges, only a few rely on discretely distributed pontoons, whereas the remainder are based on continuous pontoon girders. The majority of these bridges are also provided with additional stiffness through side-mooring. Only two long-span end-supported floating bridges exist in the world: the Bergsøysund Bridge and the Nordhordland Bridge, both relying on discretely distributed pontoons and both located in Norway. In connection with the planning of these structures, interest in the stochastic dynamic behaviour of floating bridges flourished in certain research communities, who combined the knowledge from the highly developed Norwegian offshore industry with knowledge gained during the construction of the floating bridges found in the State of Washington, USA, and in British Columbia, Canada. Much of this pioneering work can be credited to the research groups of Holand and Hartz (see, e.g., [5, 6, 7, 8, 9, 10, 11]) and Borgman [12]. The methodology was further developed, elaborated and exemplified by Sigbjörnsson [13] and by Langen and Sigbjörnsson [14].

Since the remarkable efforts contributed to the methodology in the '70s and early '80s, few case studies have been performed on real floating bridges. The effects of the flexibility of the superstructure of a pontoon bridge were studied by Kumamoto et al. [15], who emphasized the relevance of such a study in regard to the design of the Yumeshima-Maishima (Yumemai) Bridge in Osaka, Japan, around the year 2000. This unique bridge is described in [16] and is the successor to the previous massive research project concerning VLFSs in Japan: the Mega-Float. Seif and Inoue [17] performed a conceptual case study of the Bergsøysund Bridge, in which the response of the bridge was simulated in the time domain for various wave directions and spreading indices for a specified crest length.

Morris et al. [18] performed a frequency-domain analysis of the planned William R. Bennett Floating Bridge in British

*Corresponding author

Columbia. Among other relevant contributions of more recent vintage are [19] and [20].

Floating bridges play a modest role in modern infrastructure, partly because of the limited knowledge of the uncertainties that arise with increased spans. The longest existing floating bridges are moored to the seabed and rely on continuous pontoon solutions. However, individual pontoons are beneficial in many cases, and for deep straits such as fjords, it is not practically feasible to incorporate anchoring. From this kind of design follows a greater importance of the correlation of the wave action field.

An intermediate study concerning the stochastic modelling of the dynamic behaviour of the Bergsøysund Bridge was performed by Kvåle et al. [21]. The cited paper presents a similar study of the Bergsøysund Bridge; however, the current paper is far more elaborate and extensive, with respect to both the model and the interpretation of the analyses. The current paper presents a two-part combined model of the Bergsøysund Bridge, in which the fluid-structure interaction is considered using linear potential theory and the superstructure is represented by a finite element (FE) model consisting of beams and shells. The presented model serves as a basis for evaluating and discussing the damping contribution from the fluid-structure interaction. The effects of changes in the sea state, as represented by the crest length and the significant wave height, are studied in terms of both the wave excitation and the global response of the bridge. Because of the discretely distributed pontoons used in the bridge design, the wave excitation acts at only a few well-separated points. Thus, the correlation of the wave action on the bridge is an important issue and a vital aspect of this paper. With time-domain analyses in mind, the memory effect in the contribution from the fluid-structure interaction is avoided by applying two different frequency-independent approximations, and the resulting errors are discussed.

2. Outline of the theoretical model

A floating bridge is a complex structure, requiring theories from multiple scientific fields for the establishment of a complete numerical model. This section serves to outline the theoretical and mathematical framework needed for such a model. The frequency-domain equations of motion are established in Section 2.1. To solve these equations of motion with regard to the response, the power spectral density method is introduced in Section 2.2. The load acting on the structure is established through a random, Gaussian representation of the sea surface, which is established in Section 2.3 in the form of spectral densities. Furthermore, the load spectral densities are computed based on the sea surface spectral densities, as discussed in Section 2.4. To obtain a useful interpretation of the global system, a modal study is beneficial. Because of the self-exciting nature of a floating bridge, particular attention must be paid to the eigenvalue solution, as shown in Section 2.5.

2.1. Equations of motion

Within the framework of a finite element method (FEM) formulation, the equations of motion for a floating structure can be written as follows (see, e.g., Naess and Moan [22]):

$$[M_s]\{\ddot{u}(t)\} + [C_s]\{\dot{u}(t)\} + [K_s]\{u(t)\} = \{p_h(t)\} \tag{1}$$

where t is the time; $[M_s]$, $[C_s]$ and $[K_s]$ are the structural mass, damping and stiffness matrices, respectively; $\{u(t)\}$ is the displacement vector; and $\{p_h(t)\}$ is the total hydrodynamic action, including both the fluid-structure interaction and the wave action. The floating elements contribute via forces from the interaction between the water and the structure. The total hydrodynamic action can be formally expressed as follows:

$$\{p_h(t)\} = \int_{-\infty}^{\infty} [m_h(t-\tau)]\{\ddot{u}(t)\}d\tau + \int_{-\infty}^{\infty} [c_h(t-\tau)]\{\dot{u}(t)\}d\tau + [K_h]\{u(t)\} + \{p(t)\} \tag{2}$$

Here, $[m_h(t)]$ and $[c_h(t)]$ are the time-domain representations of the added hydrodynamic mass and the added hydrodynamic damping, respectively; and $\{p(t)\}$ represents the wave excitation forces. The first three terms on the right-hand side are models of the fluid-structure interaction forces. The time-domain representation of the added mass, $[m_h(t)]$, is related to the frequency-dependent hydrodynamic mass, $[M_h(\omega)]$, as follows:

$$[m_h(t)] = \frac{1}{2\pi}\int_{-\infty}^{\infty} [M_h(\omega)]e^{i\omega t}d\omega \tag{3}$$

Similarly, for the hydrodynamic damping, the following holds:

$$[c_h(t)] = \frac{1}{2\pi}\int_{-\infty}^{\infty} [C_h(\omega)]e^{i\omega t}d\omega \tag{4}$$

The restoring forces, however, are assumed to be independent of frequency. This implies that the frequency-domain and time-domain representations are identical. Here, the angular frequency is denoted by ω, and $i \equiv \sqrt{-1}$.

The wave excitation force, $\{p(t)\}$, is modelled herein as a homogeneous, stochastic, Gaussian process. The literature supports the validity of this assumption for the case of deep water and moderate wave heights (see, e.g., [23]). It follows that the response process inherits the properties of Gaussianity and homogeneity. It is assumed that the displacement and force processes can be expressed using generalized harmonic decomposition [24] as follows:

$$\{u(t)\} = \int_{-\infty}^{\infty} e^{i\omega t}\{dZ_u(\omega)\} \tag{5}$$

$$\{p(t)\} = \int_{-\infty}^{\infty} e^{i\omega t}\{dZ_p(\omega)\} \tag{6}$$

where $\{Z_u(\omega)\}$ and $\{Z_p(\omega)\}$ are the spectral processes corresponding to the response vector and the wave excitation force vector, respectively. The equations of motion can now be rewritten in the frequency domain as follows:

$$\left(-\omega^2[M(\omega)] + i\omega[C(\omega)] + [K]\right)\{dZ_u(\omega)\} = \{dZ_p(\omega)\} \tag{7}$$

The fluid-structure interaction gives rise to inertia, damping and restoring forces. Hence, the system mass, damping and restoration (stiffness) are expressed as follows:

$$[M(\omega)] = [M_s] + [M_h(\omega)] \tag{8}$$

$$[C(\omega)] = [C_s] + [C_h(\omega)] \tag{9}$$

$$[K(\omega)] = [K_s] + [K_h] \tag{10}$$

By applying linearized potential theory, numerical values can be established for the wave excitation process, the hydrodynamic restoration matrix, the frequency-dependent added damping matrix and the frequency-dependent added mass matrix. This will be further discussed in Section 2.4. For further details regarding the establishment of the equations of motion, the reader is referred to [22].

2.2. Solution technique - the power spectral density method

The probabilistic properties of the response and wave excitation processes can be fully described in terms of the cross-spectral density, provided that the mean value is zero. The cross-spectral densities of the displacement response, $\{u(t)\}$, and the wave action process, $\{p(t)\}$, can be expressed as follows [25, 13, 26]:

$$[S_u(\omega)]d\omega = E\left(\{dZ_u(\omega)\} \cdot \{dZ_u(\omega)\}^H\right) \tag{11}$$

$$[S_p(\omega)]d\omega = E\left(\{dZ_p(\omega)\} \cdot \{dZ_p(\omega)\}^H\right) \tag{12}$$

where the Hermitian operator $()^H$ is introduced to represent the complex conjugate and matrix transpose and $E()$ is the expectation operator. Combining Equations 11 and 12 with Equation 7 results in the following well-known expression:

$$[S_u(\omega)] = [H(\omega)][S_p(\omega)][H(\omega)]^H \tag{13}$$

This represents the power spectral density method and enables the computation of the response spectral densities given the spectral densities of the applied wave action.

2.3. Modelling the sea surface

The sea surface elevation is modelled as a scalar quantity given as a function of the location in space $\{x\}$ and time t, and it is an inherently random process. This is discussed in detail in Kinsman's book [27]. A thorough review of the stochastic modelling of directional seas can be found in [28]. The sea surface can be expressed mathematically in terms of the following integral:

$$\eta(\{x\}, t) = \int \exp\left(i\{\kappa\} \cdot \{x\} - i\omega t\right) dZ_\eta(\{\kappa\}, \omega) \tag{14}$$

where $\{\kappa\} = \{\kappa_x \quad \kappa_y\}$ is the wave number vector, ω is the frequency, and Z_η is the spectral process corresponding to the sea surface elevation. For stationary and homogeneous random fields, the spectral process is related to the wave spectral density as follows:

$$\begin{aligned} E\left(dZ_{\eta_r}(\{\kappa\}, \omega) dZ_{\eta_s}(\{\kappa\}, \omega)^H\right) &= dG_{\eta_r\eta_s}(\{\kappa\}, \omega) \\ &= S_{\eta_s\eta_r}(\{\kappa\}, \omega) d\kappa_x d\kappa_y d\omega \end{aligned} \tag{15}$$

where the indices r and s correspond to two points in space (and generally also time), $G_{\eta_r\eta_s}(\{\kappa\}, \omega)$ denotes the spectral distribution, and $S_{\eta_r\eta_s}(\{\kappa\}, \omega)$ is the corresponding spectral density. In polar coordinates, the wave number vector can be expressed as follows:

$$\{\kappa\} = \begin{Bmatrix} \cos\theta \\ \sin\theta \end{Bmatrix} \kappa \tag{16}$$

Here, θ refers to the wave direction and κ is the modulus of the wave number vector. Within the framework of Airy wave theory, the wave number and wave frequency are related through the dispersion relation:

$$\omega^2 = g\kappa \tanh(\kappa h) \tag{17}$$

where g is the acceleration of gravity and h is the water depth. For deep-water waves, $\tanh(\kappa h) \approx 1$. Hence, the cross-spectral density can be expressed as a function of the wave frequency and wave direction. The two-dimensional auto-spectral density is obtained from the cross-spectral density by merging the points r and s. For a homogeneous stochastic wave field, the two-dimensional wave spectral density is a function that is independent of the considered point in space:

$$S_{\eta_r\eta_r}(\omega, \theta) = S_{\eta_s\eta_s}(\omega, \theta) \tag{18}$$

This implies that the auto-spectral density can be expressed as a function of frequency and direction, i.e., $S_\eta(\omega, \theta)$; this quantity is commonly referred to as the directional wave spectral density and is traditionally written as follows:

$$S_\eta(\omega, \theta) = S_\eta(\omega) D(\omega, \theta) \tag{19}$$

where $S_\eta(\omega)$ is the so-called one-dimensional wave spectral density and $D(\omega, \theta)$ is the directional distribution. The cross-spectral density of the water elevation can then be expressed as follows for deep-water waves, under the assumption that the directional function is independent of the frequency [13]:

$$S_{\eta_r\eta_s}(\omega) = S_\eta(\omega) \int_{-\pi}^{\pi} D(\theta) \exp\left(-i\frac{|\omega|\omega}{g}(\Delta x \cos\theta + \Delta y \sin\theta)\right) d\theta \tag{20}$$

Here, Δx and Δy represent the distance between the points r and s and the mean wave direction is taken to be zero. The integral term expresses the coherency between the wave heights at the two points.

2.4. Fluid-structure interaction

The hydrodynamic forces acting on a submerged body due to a stochastic sea wave can be expressed using the following equation:

$$\{dZ_h(\omega)\} = \{dZ_p(\omega)\} - \left(-\omega^2[M_h(\omega)] + i\omega[C_h(\omega)] + [K_h]\right)\{dZ_u(\omega)\} \tag{21}$$

The vector $\{dZ_p(\omega, \theta)\}$ denotes the wave-induced process, which can be related to the wave process $dZ_\eta(\omega, \theta)$ as follows:

$$\{dZ_p(\omega, \theta)\} = \{Q_r(\omega, \theta)\} dZ_\eta(\omega, \theta) \tag{22}$$

Here, $\{Q_r(\omega,\theta)\}$ denotes the hydrodynamic transfer function that relates the wave-induced force process and the wave amplitude process, where r refers to the spatial location of an element, i.e., a pontoon. The total hydrodynamic action process $\{dZ_h(\omega)\}$ describes the fluid-structure interaction and the wave action induced by the prescribed sea state. Hydrodynamic transfer functions and fluid-structure interaction contributions are commonly established based on potential theory or experiments in wave basins. Panel methods are used to simulate the flow field around a body based on the superposition of known potential flow solutions. In this manner, simulations of the submerged body exposed to a wave of unit height with varying frequency and direction can yield both the hydrodynamic transfer functions and the hydrodynamic coefficients (mass, damping, and stiffness). The reader is referred to [29] for a thorough description of the application of potential theory to obtain these quantities. It is important to note that under the assumption of potential flow, all viscous effects are disregarded. Furthermore, potential flow methods are fundamentally based on superposition, making them linear by nature.

Finally, the cross-spectral density matrix corresponding to the wave excitation acting between two selected points can be written as follows:

$$[S_{p_r p_s}(\omega)] = \int_\theta \{Q_r(\omega,\theta)\} S_{\eta_r \eta_s}(\omega,\theta) \{Q_s(\omega,\theta)\}^H d\theta \tag{23}$$

Here, $\{Q_r(\omega,\theta)\}$ is the directional wave excitation transfer function for element r and $\{Q_s(\omega,\theta)\}$ is the directional wave excitation transfer function for element s. The matrix in Equation 23 corresponds to the six local degrees of freedom (DOFs) of points r and s and is included as a sub-matrix within the full cross-spectral density matrix corresponding to the wave excitation of all points of interest.

2.5. Eigenvalue solution

When damping is not neglected, the eigenvalues and eigenvectors become complex. The eigenvalue problem then reads as follows:

$$\left(\lambda^2[M(\omega)] + \lambda[C(\omega)] + [K]\right)\{u\} = \{0\} \tag{24}$$

Because the mass and damping matrices are non-linear functions of frequency, the eigenvalue problem is, in general, non-linear and must be solved in an iterative manner. First, the frequency dependence is disregarded. Then, Equation 24 can be re-written in state-space as follows:

$$\begin{Bmatrix}\{\dot{u}\}\\ \{\ddot{u}\}\end{Bmatrix} + \begin{bmatrix}[0] & -[I]\\ [M]^{-1}[K] & [M]^{-1}[C]\end{bmatrix}\begin{Bmatrix}\{u\}\\ \{\dot{u}\}\end{Bmatrix} = \begin{Bmatrix}\{0\}\\ [M]^{-1}\{p\}\end{Bmatrix} \tag{25}$$

In condensed form, this reads as follows:

$$\{\dot{z}\} + [A]\{z\} = \{Q\} \tag{26}$$

This results in the following solution for the state-space variable:

$$\{z\} = \sum_{r=1}^{2N} \{q_r\} e^{\lambda_r t} \tag{27}$$

Table 1: Pseudocode of the iterative algorithm used to solve the eigenvalue problem.

```
INPUT N, tolerance
FOR n = 1 to 2N
    ω = 0
    diff = tolerance + 1
    WHILE diff > tolerance
        Solve eigenvalue problem for chosen ω ⇒ λ_r and {q_r}
        Sort λ_r, and correspondingly sort {q_r}
        ω_0 = ω
        ω = |λ_n|   (n = r)
        diff = |ω_0 − ω|
    END
    Store eigenvalue λ_n = λ_r and eigenvector {q_n} = {q_r}
END
```

where $\{q_r\}$ and λ_r are the eigenvector and eigenvalue, respectively, corresponding to solution r of Equation 26. It is assumed that the eigenvalues are sorted such that $\{q_{r+N}\}$ and λ_{r+N} are complex conjugates of $\{q_r\}$ and λ_r, respectively. This can further be re-written in this compact manner, representing the displacements only:

$$\{u\} = [\Psi]\{g\} \tag{28}$$

where $[\Psi]$ is the modal transformation matrix that contains the complex mode shapes and $\{g\}$ represents the generalized DOFs.

Because of the frequency dependency of the matrices that form the eigenvalue problem, it is a non-linear problem, which, in this case, is solved by iteration. The iterative procedure used for this purpose is illustrated by the pseudocode presented in Table 1. The main workings of this algorithm are identical to those of the algorithms used to solve similar problems related to the wind loads on suspension bridges, as described by Agar [30].

The eigenvalues for an under-critically damped and frequency *in*dependent SDOF problem are as follows:

$$\lambda_r = -\xi_r\omega_r \pm \sqrt{1-\xi_r^2}\,\omega_r i \tag{29}$$

This results in the following well-known relations:

$$\omega_r = |\lambda_r| \tag{30}$$

$$\xi_r = -\frac{\Re(\lambda_r)}{|\lambda_r|} \tag{31}$$

where ω_r and ξ_r are the undamped natural frequency and the critical damping ratio, respectively, of mode r.

3. Case study: The Bergsøysund Bridge

The Bergsøysund Bridge is a 931 m long floating bridge that crosses the strait between Aspøya and Bergsøya, located on the northwestern coast of Norway. This bridge consists of a steel truss supported by 7 discretely distributed light-weight concrete pontoons, as shown in Figure 1 and Figure 2. The geography surrounding the bridge is depicted in the map shown in Figure

Figure 1: The Bergsøysund Bridge. Photograph: K. A. Kvåle.

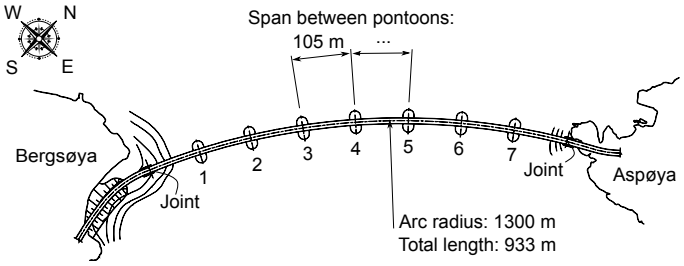

Figure 2: Overhead view of the Bergsøysund Bridge, including the chosen pontoon numbering.

3. As indicated in Figure 4, the depth of the strait at all pontoon locations except one is approximately equal to or greater than 100 meters; therefore, it is reasonable to model the problem using deep-water waves. No mooring is present, which makes this bridge a very interesting case study: the Bergsøysund Bridge is one of the longest end-supported floating bridges in the world.

3.1. Two-part combined model

In the computational set-up, which is illustrated in Figure 5, the problem is divided into two sub-structures: (i) an Abaqus FE model representing all structural contributions, including the inertia of the pontoons themselves and the constant buoyancy provided by the pontoons, and (ii) a DNV HydroD WADAM hydrodynamic model, excluding static contributions due to gravity and hydrostatics.

The FE model consists of the steel frame and the tension rods at both abutments, both represented by linear beam elements, as well as the bridge deck, represented by shell elements. A rendering of this model is shown in Figure 6. The neoprene bearings at the ends of the bridge are modelled as linear springs.

The hydrodynamic contributions are considered separately for each pontoon. The pontoons are modelled with their natural waterlines near those indicated in the design plans for the bridge.

The set-up of the model is described step by step below, corresponding to the numbering indicated in Figure 5:

1. The beams and shells in the FE model define the structural system matrices $[M_s]$ and $[K_s]$. Additionally, the inertia of the mass of the pontoons themselves, $[M_{h0}]$, and the frequency-independent buoyancy (stiffness) from the hydrodynamic model, $[K_h]$, are included. Note that the stiffness contributions corresponding to each pontoon, $[K_{h,i}]$, must be transformed and summed; both of these tasks are performed in the FE software.

Figure 3: Map section showing the geography surrounding the bridge. © Kartverket (`www.kartverket.no`). Two map sections from Kartverket are combined in this figure.

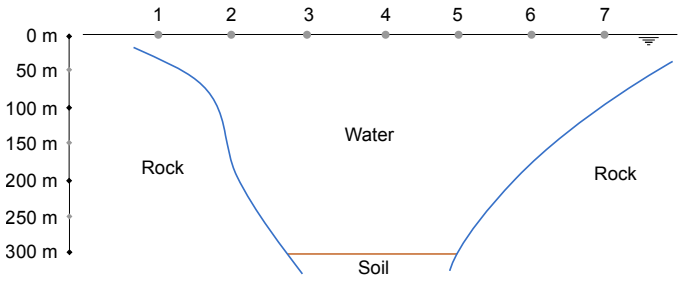

Figure 4: Water depth profile across the strait, with annotations indicating pontoon locations.

2. A modal analysis of the FE model is performed, yielding the modal transformation matrix, $[\Phi^I]$, and the natural frequencies, ω_n^I.
3. The modal quantities are used to establish the modal system matrices, $[\tilde{M}^I]$ and $[\tilde{K}^I]$, corresponding to a preselected number of vibration modes. Rayleigh damping is enforced to establish the modal damping matrix, $[\tilde{C}^I]$, with mass and stiffness proportionality constants of $\alpha = \beta = 5 \cdot 10^{-3}$. The assumed values of these parameters correspond to a very lightly damped steel structure, i.e., with damping in the range of 0.5 to 1.0% of critical damping.
4. The seven pontoons of the bridge can be classified into three types (1 and 7; 2 and 6; 3, 4 and 5) based on the physical properties arising from their geometries and ballasting; thus, three different pontoon models are needed. The hydrodynamic stiffness contributions from each pontoon are not included here because they are considered as part of the FE model. The hydrodynamic mass and damping matrices representing the contributions of the individual pontoons are therefore the only contributions that are considered as part of sub-structure II. The discretization used for the hydrodynamic system matrices is provided in Table 2.
5. To form the total mass and damping contributions, the pontoon-wise matrices corresponding to sub-structure II are transformed into the global DOFs and summed.
6. The global mass and damping from sub-structure II are transformed into the modal space defined by sub-structure I using the modal transformation matrix $[\Phi^I]$.
7. The total modal system matrices are established by summing the contributions from sub-structures I and II. These matrices are used to establish the modal frequency-domain transfer function, $[\tilde{H}(\omega)]$.
8. The numerical functions for the one-dimensional wave spectral density and the spreading function are established based on the chosen models (in this case, the one-parameter Pierson-Moskowitz spectrum for the one-dimensional wave spectral density and cos-2s for the spreading function). The numerical two-dimensional wave spectral density is established.
9. Based on the same three hydrodynamic analyses as those used to establish the hydrodynamic mass, damping and stiffness, the hydrodynamic transfer function, $\{Q_r(\omega, \theta)\}$, is established. The discretization used for the hydrodynamic transfer function is provided in Table 2.
10. Equation 23 is solved numerically for all combinations of pontoons (7^2). At this point, the hydrodynamic transfer function is transformed into the global coordinate system.
11. The sub-matrices are stacked to form the total load spectral density matrix.
12. The load spectral density matrix is transformed into the modal space defined by sub-structure I.
13. The power spectral density method (Equation 13) is used to establish the displacement spectral densities.
14. Finally, the response spectral density is transformed from modal into physical DOFs.

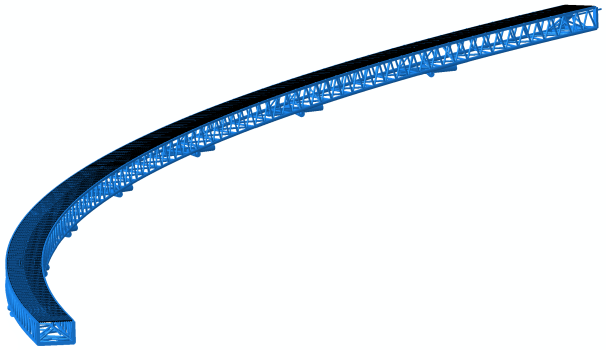

Figure 6: Rendering of the FE model.

Table 2: Properties of the discretization used in the hydrodynamic analysis. The angle is defined as the angle between the positive local x axis of the pontoon and the wave direction.

Variable	Range	Increment	Affected quantities
Freq. [rad/s]	$[7.5 \cdot 10^{-2}, 4]$	$7.5 \cdot 10^{-2}$	$\{Q_r(\omega, \theta)\}$, $[M_h(\omega)]$, $[C_h(\omega)]$
Angle [°]	[0,350]	10	$\{Q_r(\omega, \theta)\}$

3.2. *Modal parameters*

By employing the algorithm introduced in Table 1, the frequency-dependent eigenvalue problem was solved, yielding the natural frequencies, damping estimates and mode shapes. The natural frequencies presented are the undamped ones. The resulting mode shapes were used to sort the modes according to their displacement type into horizontally transversal (H), vertically transversal (V), torsional (T), and combinational (C) modes. The natural frequencies and critical damping ratios for 10 selected modes are presented in Table 3, and the corresponding mode shapes are presented in Figure 7.

The critical damping ratios of modes near 1 rad/s are found to be close to 12%. Compared with land-based steel structures, this ratio is very high. In the context of systems with significant hydrodynamic contributions, however, these damping values are not abnormally high. The high damping will affect the response spectral densities and result in blunt peaks at frequen-

Table 3: Undamped natural frequencies (and periods) and damping ratios obtained from the eigenvalue solution.

	Period	Frequency		Damping	
Mode no.	T [s]	ω [rad/s]	f [Hz]	ξ [%]	Type
1	10.7498	.5845	0.0930	1.792	H
2	7.1048	.8844	0.1408	1.298	C
3	6.1071	1.029	0.1637	11.80	V
4	5.9411	1.058	0.1683	10.66	V
5	5.2002	1.208	0.1923	7.418	C
6	5.1062	1.231	0.1958	9.234	H
7	4.3032	1.460	0.2324	3.155	V
8	3.8206	1.645	0.2617	1.115	T
9	3.3254	1.890	0.3007	6.696	H
10	3.3201	1.893	0.3012	1.078	V

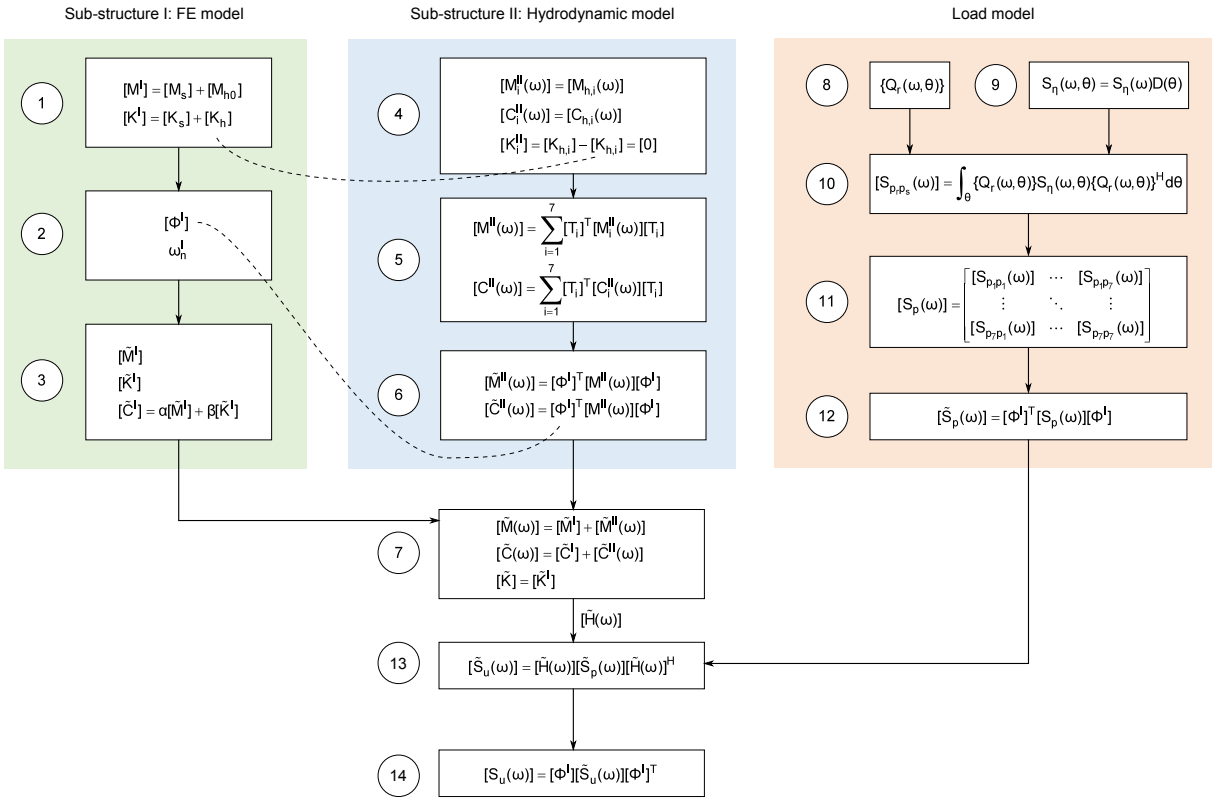

Figure 5: Basic structure of the calculation set-up. The sub-index $_{h0}$ corresponds to the frequency-independent contributions from the hydrodynamic model; the superindices ^{I} and ^{II} correspond to sub-structures I and II, respectively; and $\sim$ indicates modal quantities.

cies corresponding to these modes.

Additionally, the critical damping ratios and natural frequencies for all eigenvalues between 0 and 3 rad/s are presented in Figure 8, along with the assessed Rayleigh damping mentioned above. From this figure, it is evident that hydrodynamic frequency-dependent damping contributes strongly to the overall damping of the structure. Upon investigation, Figure 8 also shows that the damping ratios are clearly dependent on the type of mode. Notably, mode 9 has a significantly higher frequency than mode 6, despite their similarity. This is explained by the fact that mode 9 also includes a translational movement, resulting in a higher strain energy and, consequently, a higher frequency.

3.3. Load modelling

The hydrodynamic analysis yielded the discretized directional wave excitation transfer function $\{q_r(\omega,\theta)\}$, introduced in Equation 23. Figure 9 shows the transfer function vector for the middle pontoon in the model. The discretization used for the hydrodynamic transfer function is presented in Table 2.

The one-parameter Pierson-Moskowitz wave spectral density suggested in [31] was used as the one-dimensional wave spectral density in the current case study. In this spectral density, the parameters of the generalized Pierson-Moskowitz spectral density are represented in terms of the significant wave height H_s as follows:

$$S_\eta(\omega) = \frac{A}{\omega^4} \cdot \exp\left(\frac{-B}{\omega^5}\right) \tag{32}$$

where $A = \alpha g^2$, $B = 3.11/H_s^2$, $\alpha = 0.0081$, and g is the acceleration of gravity. The significant wave height H_s is defined as the mean wave height of the highest third of the wave (in a time series), which is often denoted by $H_{1/3}$. Furthermore, the significant wave height is related to the variance of the wave height process as follows: $H_s = 4\sigma_\eta$. The relationship between the peak wave period and the significant wave height in this spectral density model is plotted in Figure 17 together with the measured data from a report by Veritec [32] regarding the sea state at the bridge site. This figure supports the assertion that this spectral density formulation is appropriate for the current case study.

The cos-2s distribution [33] was selected as the directional distribution $D(\theta)$:

$$D(\theta) = C\cos^{2s}\left(\frac{\theta - \theta_0}{2}\right) \tag{33}$$

where C is a normalization constant to ensure that $\int D(\theta)d\theta = 1$; s is the spreading parameter, which characterizes the crest length of the waves; θ_0 is the angle of the mean wave direction; and θ is assumed to lie within the range corresponding to valid states of the modelled sea state, i.e., $-\pi/2 < \theta - \theta_0 < \pi/2$. The

(a) $\omega_1 = 0.5845$ rad/s

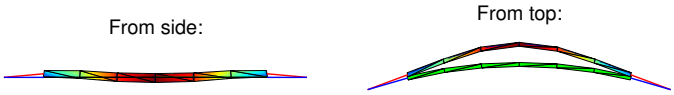

(b) $\omega_2 = 0.8844$ rad/s

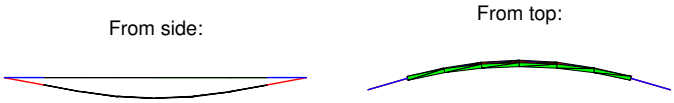

(c) $\omega_3 = 1.029$ rad/s

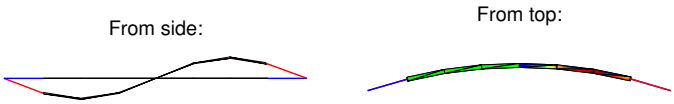

(d) $\omega_4 = 1.058$ rad/s

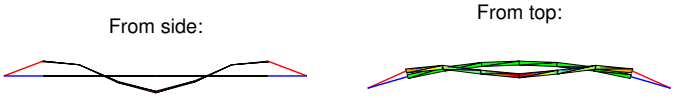

(e) $\omega_5 = 1.208$ rad/s

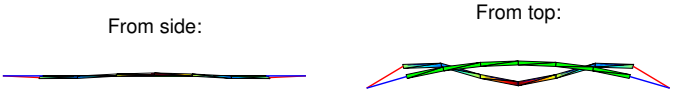

(f) $\omega_6 = 1.231$ rad/s

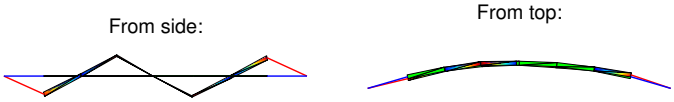

(g) $\omega_7 = 1.460$ rad/s

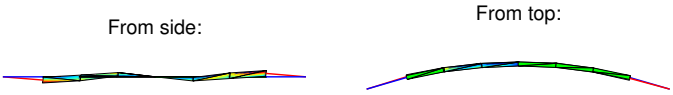

(h) $\omega_8 = 1.645$ rad/s

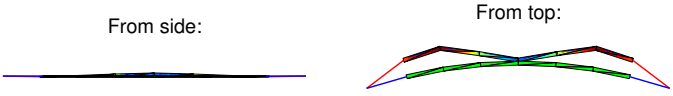

(i) $\omega_9 = 1.890$ rad/s

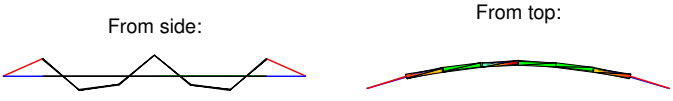

(j) $\omega_{10} = 1.893$ rad/s

Figure 7: Mode shapes obtained from the eigenvalue problem, corresponding to the natural frequencies and critical damping ratios presented in Table 3 and Figure 8.

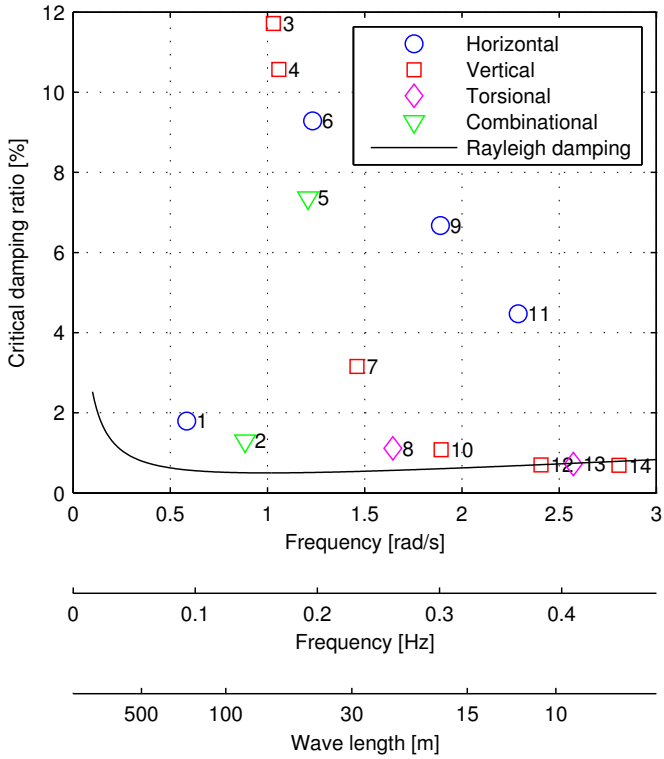

Figure 8: Undamped natural frequencies and critical damping ratios obtained from the eigenvalue solution. The wavelength scale was constructed using Airy wave theory. The Rayleigh curve refers to the global damping added to the dry part of the structure and is not to be interpreted as a result of the eigenvalue solution.

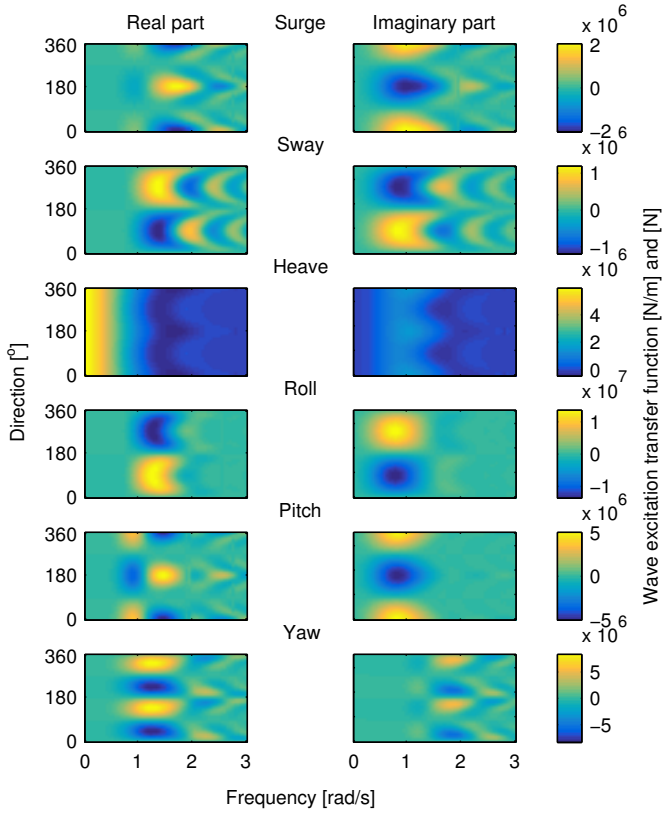

Figure 9: Wave excitation transfer function for the middle pontoon obtained in the hydrodynamic analysis, where the rows correspond to the local degree of freedom as follows (from the top): x, y, z, θ_x, θ_y, and θ_z. The left column represents the real part, and the right column represents the imaginary part.

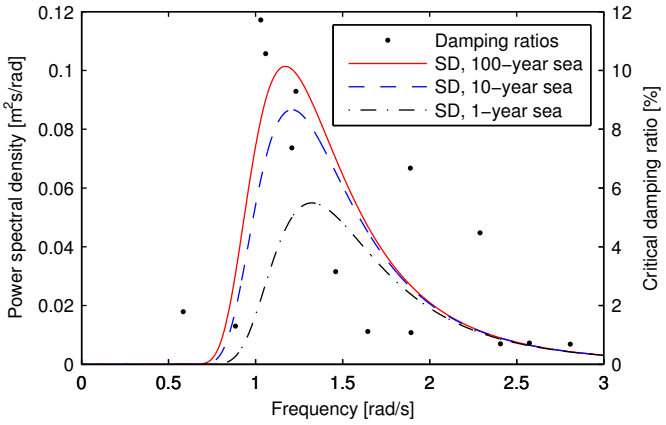

Figure 10: Damping ratios and one-parameter Pierson-Moskowitz wave spectral densities corresponding to sea states of given return periods: H_s = 1.41 m for the 100-year sea state, H_s = 1.15 m for the 10-year sea state, and H_s = 0.90 m for the 1-year sea state [32].

mean wave angle, defined as the angle between the global x axis and the local y axis of the midmost pontoon, was chosen such that the bridge was symmetrically loaded, i.e., 90°.

The resulting directional distributions, for a mean angle of 90° and various spreading parameters, are shown in Figure 11.

3.4. Sea-state effects

Changes in the spreading parameter s, the significant wave height H_s and the mean wave heading angle θ_0 directly affect the excitation of the structure. The effects on the response, particularly the correlation between response quantities, are more complex. Parameter studies based on simulations were performed to assess the effect of the parameters that characterize the sea state on the response.

3.4.1. Significant wave height

For the one-dimensional Pierson-Moskowitz spectral density used in this study, an increase in the significant wave height results in a lower peak frequency of the spectral density. This will, in turn, result in a higher excitation level and a lower peak frequency of the wave action. This effect is illustrated in Figure 10 for significant wave heights corresponding to 1-year, 10-year and 100-year sea states, as reported in [32], together with the modal damping ratios and natural frequencies from the eigenvalue solution. From this figure, it is clear that the peak

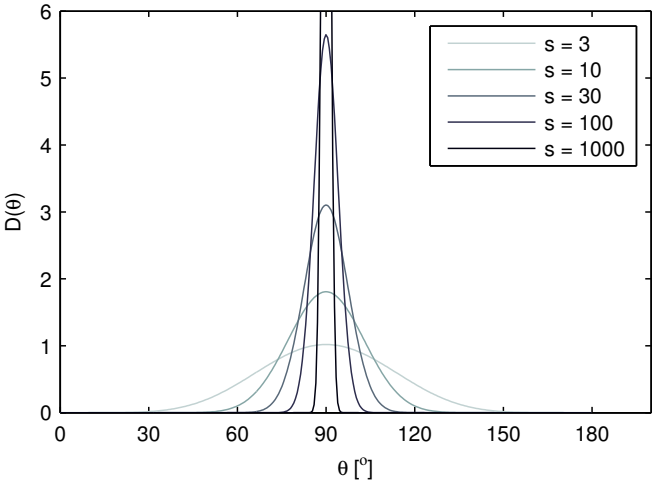

Figure 11: The applied $\cos^{2s}$-based directional distribution, with a mean heading angle of 90°, for various spreading parameters.

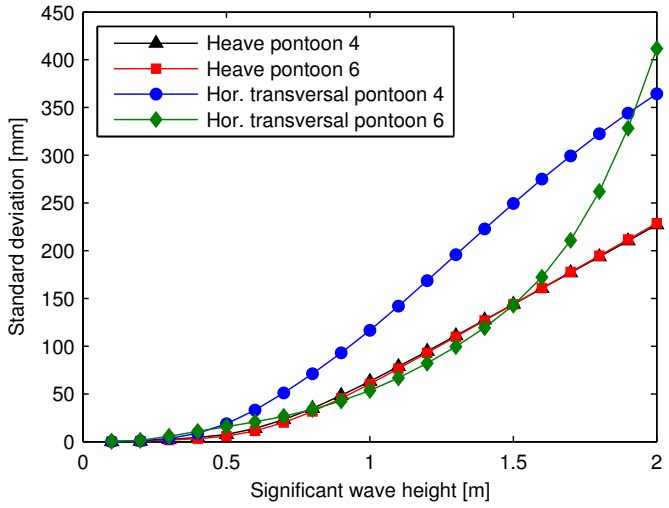

Figure 12: Effects on the variance of selected responses with an increasing significant wave height for a spreading parameter of $s = 3$ and a mean wave heading angle of $\theta_0 = 90^o$.

frequency of the wave action and the modes with the highest damping correspond better for higher significant wave heights. This means that for higher significant wave heights, the more highly damped modes are more strongly excited and therefore contribute more significantly to the overall response than in the case of lower significant wave heights. The high damping plays a crucial role in limiting the response of the structure, but high damping levels should not be regarded as strictly beneficial; high damping affects the correlations between the responses at different locations in the structure, potentially leading to larger local stress variations. During the design of a floating bridge, this effect should be taken into consideration.

The response was simulated for various significant wave heights. The resulting standard deviations of the heave motion and horizontally transversal motion of pontoons 4 and 6 are shown in Figure 12. This figure reveals a significant increase in the horizontally transversal response of pontoon 6 as the significant wave height increases. This increase in response originates from the excitation of the first mode of vibration, the mode shape of which is presented in Figure 7a. As the significant wave height increases, the frequency content of the wave excitation process will shift downwards, as shown in Figures 10 and 17. This shift in frequency content excites the first vibrational mode, which is otherwise located in the low-level tail of the one-dimensional wave spectral density, and, in turn, significantly affects the response.

3.4.2. Crest length

The crest length is controlled by the spreading parameter s that appears in the directional distribution. In the current case study, the spreading parameter s was selected based on quantitative judgement and site observations. To obtain a more accurate measure of this quantity, wave recordings would be needed; however, such an effort is considered to be outside the scope of this study. The three values used for s in this survey (3, 30 and 1000) are considered to represent *short-crested*, *fairly long-crested* and *long-crested* sea conditions. Particular attention is focused on the value of $s = 3$, as on-site observations imply that a short-crested representation is the most realistic. To more clearly illustrate the effect of the spreading parameter on the sea surface, representations of the sea surface for $s = 3$, $s = 30$, and $s = 1000$ are shown in Figures 13-15. The correlations between the wave height at the midmost pontoon and those along the rest of the bridge are shown in the same figures for the corresponding sea states.

These figures show that the correlations between the wave heights are very low; only when the waves are long-crested is there a non-zero wave-height correlation between neighbouring pontoons. As a result of the low correlation between the wave heights, the cross-spectral densities between the wave excitations of the different pontoons are very small and can be neglected for the types of sea states assumed at the bridge location. Note that the correlation plots are also highly dependent on the chosen one-dimensional wave spectral density. As the significant wave height, which controls the form of the wave spectral density, increases, the highly correlated region expands dramatically in the directions both parallel and normal to the wave propagation.

The significant wave heights in the locations of other potential floating bridges may be far larger than those measured around the Bergsøysund Bridge, and therefore, it is important to understand the correlations between wave actions on different pontoons.

By simulating the responses for various spreading parameters, the statistics of the responses in various DOFs of the model were established. The standard deviations of the heave motion and horizontally transversal motion of pontoons 4 and 6 for varying s are shown in Figure 16. This plot reveals a decrease in the response in terms of the horizontally transversal motion and an increase in the vertical motion. As the sea surface becomes more long-crested, the wave-excitation correlation increases; the pontoons are excited more simultaneously. This will, in turn, increase the response of the symmetric modes; however, it may also reduce the intensity of the antisymmetric modes of vibration. This is the cause of the somewhat unexpected behaviour in response to an increased crest length observed in the figure.

3.5. Bridge response due to typical sea state

The one-year sea state reported by Veritec, represented by a significant wave height of $H_s = 0.90$ m, is considered in the following. Furthermore, the crest length is chosen to be characterized by a spreading parameter of $s = 3$.

Figures 18 and 19 present the resulting power spectral densities and coherences of the responses in the vertical and horizontal directions, respectively, for pontoons 3, 4 and 5; the corresponding statistics are summarized in Tables 4 and 5. The response spectral densities are represented with respect to the local DOFs of pontoon 4. The vertical displacement responses are found to have low correlation values in general, a finding that is supported by the low coherence values between the vertical responses at the natural frequencies of the vertical modes

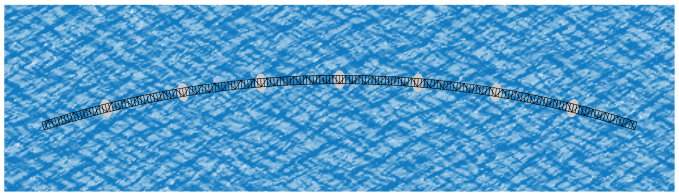

(a) Sea surface representation.

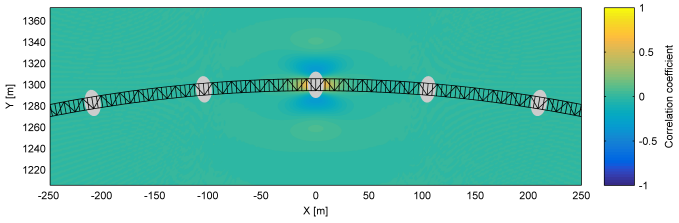

(b) Correlation with the wave height at the midmost pontoon.

Figure 13: Sea surface representation and correlation with the wave height at the midmost pontoon for a sea state characterized by $H_s = 0.9$ m, $\theta_0 = 90^o$ and $s = 3$.

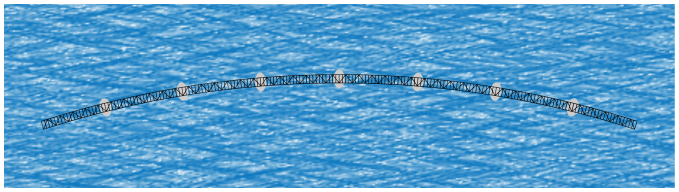

(a) Sea surface representation.

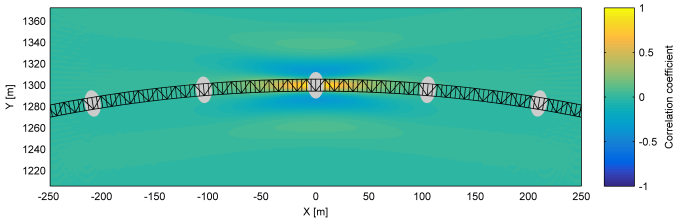

(b) Correlation with the wave height at the midmost pontoon.

Figure 14: Sea surface representation and correlation with the wave height at the midmost pontoon for a sea state characterized by $H_s = 0.9$ m, $\theta_0 = 90^o$ and $s = 30$.

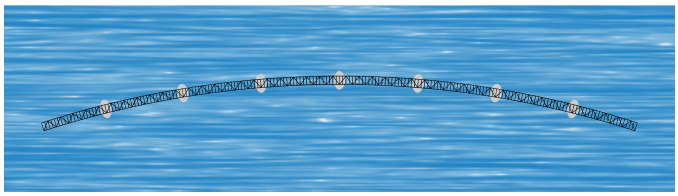

(a) Sea surface representation.

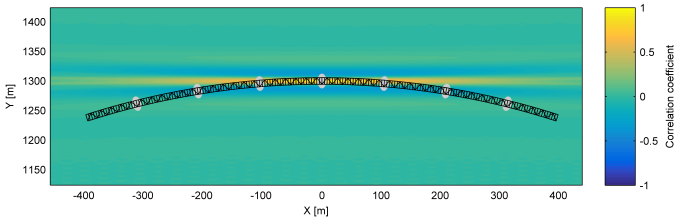

(b) Correlation with the wave height at the midmost pontoon.

Figure 15: Sea surface representation and correlation with the wave height at the midmost pontoon for a sea state characterized by $H_s = 0.9$ m, $\theta_0 = 90^o$ and $s = 1000$.

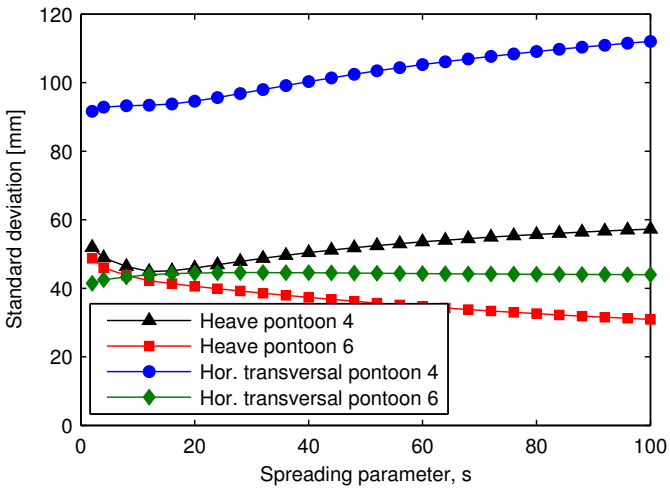

Figure 16: Effects on the variance of selected responses with an increasing spreading parameter (and thus an increasing crest length) for a significant wave height of $H_s = 0.9m$ and a mean wave heading angle of $\theta_0 = 90^o$.

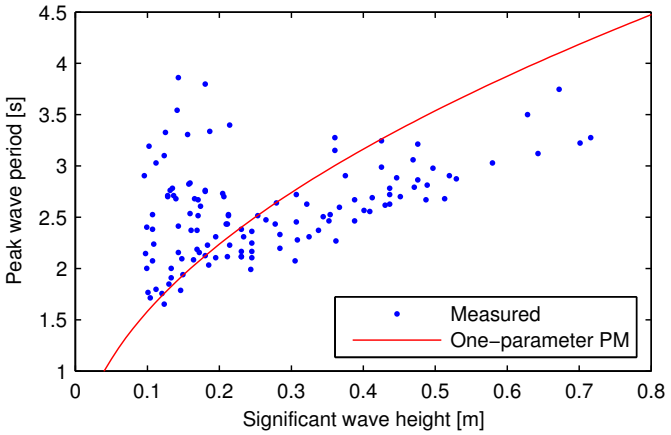

Figure 17: Measurements of significant wave heights and wave peak periods, from the Veritec report [32], compared with the relation given by the one-parameter Pierson-Moskowitz (PM) spectral density used in the study.

Table 4: Covariances [mm^2] and correlation coefficients (above the diagonal) for the heave responses of the three midmost pontoons. The statistics correspond to Figure 18.

	Pontoon 3	Pontoon 4	Pontoon 5
Pontoon 3	1959	0.640	0.0825
Pontoon 4	1373	2345	0.640
Pontoon 5	161.5	1373	1959

of the bridge. The spectra that show the horizontal displacement responses do not share this tendency: high coherence is observed at and around the peaks representing the natural frequencies of the horizontal modes of the structures, and the horizontal response variables exhibit high correlations. The inconsistencies in the damping ratios between the horizontal and vertical modes, as shown in Figure 8, are likely the cause of this result.

3.6. Simplified frequency-independent hydrodynamic model

When general non-linearities are added to the problem, a time-domain representation is close to inevitable. To properly include the fluid-structure interaction, convolution integrals must be solved, which is considered to be a computationally expensive procedure. For this reason, approximations of the frequency-dependent coefficients as constant have received some attention in the literature. The success of simplifying the frequency-dependent hydrodynamic coefficients as independent of frequency is highly dependent on the wave action process; a narrow-banded process with a long characteristic period is much more likely to

Table 5: Covariances [mm^2] and correlation coefficients (above the diagonal) for the horizontally transverse responses of the three midmost pontoons. The statistics correspond to Figure 19.

	Pontoon 3	Pontoon 4	Pontoon 5
Pontoon 3	3919	0.897	0.702
Pontoon 4	5225	8662	0.897
Pontoon 5	2752	5224	3919

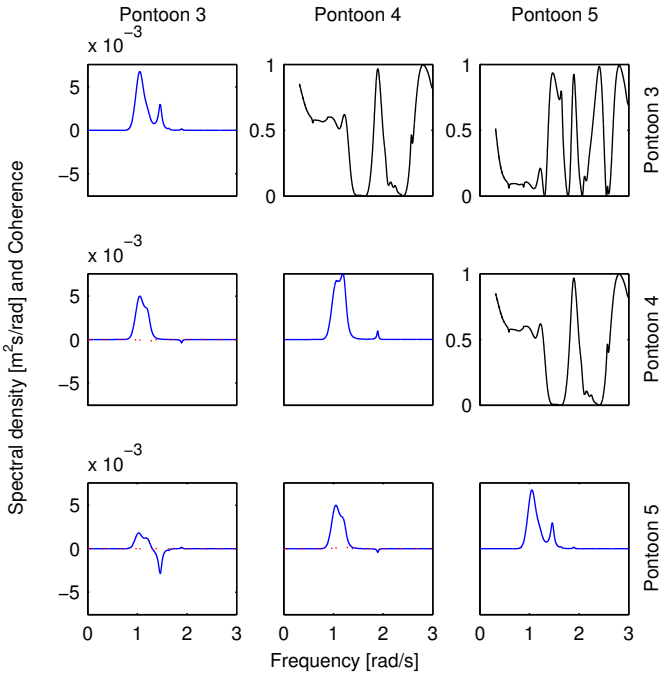

Figure 18: Cross-spectral densities of the heave responses of the three midmost pontoons. The three black curves shown above the diagonal represent the coherence between the responses, and the blue and red/dotted curves denote the real and imaginary parts of the cross-power spectral densities, respectively.

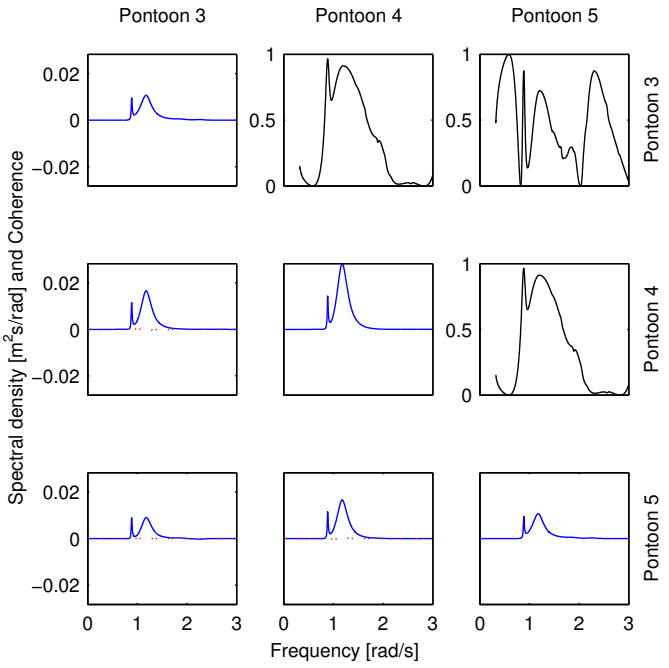

Figure 19: Cross-spectral densities of the horizontally transversal responses of the three midmost pontoons. The three black curves shown above the diagonal represent the coherence between the responses, and the blue and red/dotted curves denote the real and imaginary parts of the cross-power spectral densities, respectively.

be amenable to this type of simplification. Several procedures for this purpose have been suggested, but the emphasis here is placed on approximating the frequency-dependent coefficients as constant based on their values at (i) the peak frequency corresponding to the one-dimensional wave spectral density and (ii) the weighted average frequency corresponding to the maximum peaks of the auto-spectral densities of the response, based on an exact frequency-domain solution. The weighted average of approximation (ii) is computed as follows:

$$\omega_{tot} = \frac{1}{\sum_{i=1}^{N} W_i} \sum_{i=1}^{N} W_i \cdot \omega_i \tag{34}$$

Here, the frequency corresponding to the largest value of the auto-spectral density $S_{i,i}(\omega)$ is denoted by ω_i, N is the total number of DOFs, and the weighting coefficients W_i are defined as follows:

$$W_i = \sqrt{\max\left(S_{i,i}(\omega)\right)} \tag{35}$$

A comparison of the standard deviations and correlation coefficients corresponding to the heave and horizontally transversal responses of pontoons 3 and 4 is presented in Table 6. To complement this table, the corresponding spectral densities are presented in Figure 20. Both the figure and the table show that the second approach generally outperforms the first. However, the results obtained using both procedures are rather crude, their greatest shortcoming being that they both underestimate and overestimate the response and the correlations.

4. Concluding remarks

The potential of floating bridges for application as part of modern infrastructure is not fully utilized today, primarily due to the limited knowledge of their dynamic behaviours as their lengths are increased. Linear frequency-domain simulations were performed in a case study of the 23-year-old Bergsøysund Bridge in Norway, with emphasis on the response spectral densities determined using the power spectral density method and the modal parameters resulting from the complex and non-linear eigenvalue problem. The effects of different sea states and how they affect the response of the bridge were discussed.

The high damping contribution from the fluid-structure interaction results in low coherence and correlation between the heave response quantities along the bridge span. With damping levels as high as 12% for lateral modes, this result is as expected.

For a realistic 1-year sea state, a low correlation between the wave heights at the locations of the different pontoons was found; the action on each pontoon can therefore be considered independent. When the significant wave height increases to higher levels, however, the pontoons are exposed to correlated wave excitation. The correlation of the wave action amplifies the response of the modes with symmetric properties but may reduce the response of the antisymmetric modes. The geometry of the bridge also plays a crucial role in how strongly correlated the pontoon action becomes. Because the first mode of vibration has a frequency located in the tail of the

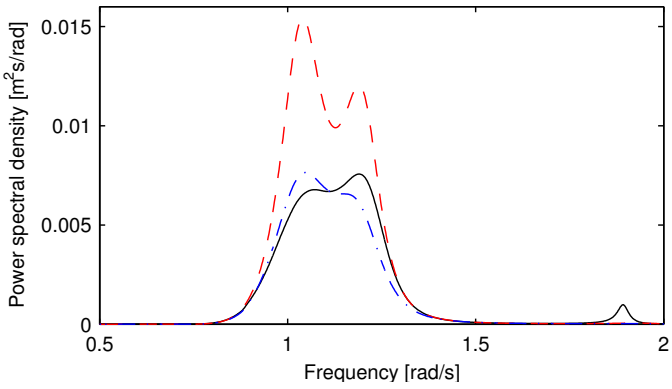

(a) Heave component.

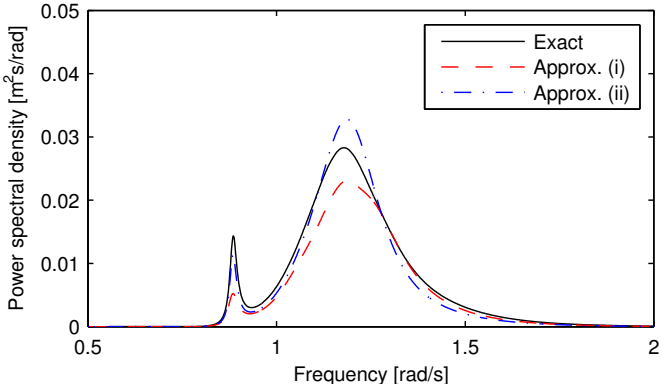

(b) Horizontally transversal component.

Figure 20: Comparison of spectral densities obtained from exact and approximate solutions.

Table 6: Comparison of the standard deviations determined through exact computation with the standard deviations obtained using two different constant approximations of the frequency-dependent mass and damping matrices corresponding to the fluid-structure interaction. Approximation (i) uses the values of the matrices at the frequency corresponding to the peak of the one-dimensional wave spectral density, whereas approximation (ii) utilizes the matrix values at the average of the square-root-weighted frequencies corresponding to the peaks of the response spectral density obtained from an exact frequency-domain solution.

		Standard deviation [mm]			Correlation coefficient		
Component	Pontoon	Exact	Approx. (i)	Approx. (ii)	Exact	Approx. (i)	Approx. (ii)
Heave	No. 3	44.26	56.42	42.76	0.640	0.716	0.700
	No. 4	48.43	61.34	46.75			
Horizontal	No. 3	62.60	58.15	61.81	0.897	0.876	0.883
	No. 4	93.07	84.46	91.31			

one-dimensional wave spectral density for low and medium significant wave heights, its contribution to the global behaviour requires a rather large significant wave height.

The approximation of the fluid-structure interaction contributions as constant for a frequency corresponding to the weighted average frequency of the peak auto-spectral densities obtained from an exact frequency-domain solution, termed approximation (ii), performed decently for a realistic 1-year sea state. The performance of this approximation is expected to be significantly enhanced when the wave excitation process is less broadband in nature. The constant approximation of the frequency-dependent fluid-structure interaction contributions lacks consistency; it both underestimates and overestimates the response and must therefore be used with caution.

Verification of the calculation models used for floating bridges is important to ensure reliable analyses. To verify the model and quantify its uncertainties, experimental data regarding the behaviour of the bridge should be recorded and analyzed.

ACKNOWLEDGEMENTS

This research was conducted with financial support from the Norwegian Public Roads Administration. The authors gratefully acknowledge this support. Thanks are also given to the master's students who have contributed to the project.

REFERENCES

[1] E. Watanabe, Floating bridges: past and present, Structural Engineering International 13 (2) (2003) 128–132.

[2] C. M. Wang, E. Watanabe, T. Utsunomiya, Very large floating structures, CRC Press, 2007.

[3] C. M. Wang, B. T. Wang, Large Floating Structures: Technological Advances, Vol. 3, Springer, 2014.

[4] G. Moe, Design philosophy of floating bridges with emphasis on ways to ensure long life, Journal of Marine Science and Technology 2 (3) (1997) 182–189.

[5] I. Holand, I. Langen, Salhus floating bridge: theory and hydrodynamic coefficients, SINTEF Rep.

[6] I. Holand, I. Langen, Dynamic Analysis of Floating Bridges, in: P. Aune, I. Holand (Eds.), Norwegian Bridge Building, Tapir Publishers, Trondheim, 1981.

[7] D. Clough, R. Sigbjornsson, S. N. Remseth, Response of a submerged, buoyant tubular bridge subjected to irregular sea waves, SINTEF Rep. 71 (1977) A77028.

[8] I. Langen, Frequency domain analysis of a floating bridge exposed to irregular short-crested waves, SINTEF Rep. (1980) ii,61 bl.

[9] B. J. Hartz, B. Mukherji, Dynamic response of a floating bridge to wave forces, in: Proc. International Conference on Bridging Rion-Antirion. Patras, Greece, 1977.

[10] B. J. Hartz, Dynamic Response of the Hood Canal Floating Bridge, in: Proceedings Second ASCE/EMD Specialty Conference on Dynamic Response of Structures, Atlanta, GA, 1981.

[11] B. J. Hartz, C. Georgiadis, A finite element program for dynamic response of continuous floating structures in short-crested waves. (1982). URL http://www.scopus.com/inward/record.url?eid=2-s2.0-0019936983&partnerID=tZOtx3y1

[12] L. E. Borgman, Ocean wave simulation for engineering design, Tech. rep. (1967).

[13] R. Sigbjörnsson, Stochastic theory of wave loading processes, Engineering Structures 1 (2) (1979) 58–64. doi:http://dx.doi.org/10.1016/0141-0296(79)90014-2.
URL http://www.sciencedirect.com/science/article/pii/0141029679900142

[14] I. Langen, R. Sigbjörnsson, On stochastic dynamics of floating bridges, Engineering Structures 2 (4) (1980) 209–216. doi:http://dx.doi.org/10.1016/0141-0296(80)90002-4.
URL http://www.sciencedirect.com/science/article/pii/0141029680900024

[15] N. Kumamoto, T. Maruyama, Elastic response analysis method for floating bridges in waves, Tech. rep. (1999).

[16] E. Watanabe, T. Maruyama, H. Tanaka, S. Takeda, Design and construction of a floating swing bridge in Osaka, Marine Structures 13 (4-5) (2000) 437–458. doi:10.1016/S0951-8339(00)00016-2.
URL http://www.sciencedirect.com/science/article/pii/S0951833900000162

[17] M. S. Seif, Y. Inoue, Dynamic analysis of floating bridges, Marine Structures 11 (12) (1998) 29–46. doi:http://dx.doi.org/10.1016/S0951-8339(97)00012-9.
URL http://www.sciencedirect.com/science/article/pii/S0951833997000129

[18] E. Morris, V. Szabo, G. Yang, M. Isaacson, Frequency Domain Dynamic Analysis of a Floating Bridge, Coastal Structures 2003 (2004) 1334–1346doi:doi:10.1061/40733(147)110.
URL http://dx.doi.org/10.1061/40733(147)110

[19] F. Shixiao, C. Weicheng, C. Xujun, W. Cong, Hydroelastic analysis of a nonlinearly connected floating bridge subjected to moving loads, Marine Structures 18 (1) (2005) 85–107. doi:10.1016/j.marstruc.2005.05.001.
URL http://www.sciencedirect.com/science/article/pii/S0951833905000377

[20] I. G. Raftoyiannis, T. P. Avraam, G. T. Michaltsos, Analytical models of floating bridges under moving loads, Engineering Structures 68 (2014) 144–154. doi:10.1016/j.engstruct.2014.03.002.
URL http://linkinghub.elsevier.com/retrieve/pii/S0141029614001400

[21] K. A. Kvåle, O. Øiseth, R. Sigbjörnsson, Modelling of the stochastic dynamic behaviour of the Bergsøysund Bridge, in: A. Logg, K.-A. Mardal, A. Massing (Eds.), Proceedings of the 26th Nordic Seminar on Computational Mechanics, Oslo, 2013, pp. 100–103.

[22] A. Naess, T. Moan, Stochastic dynamics of marine structures, Cambridge University Press, New York, 2012.

[23] M. K. Ochi, W.-C. Wang, Non-Gaussian characteristics of coastal waves,

Coastal Engineering Proceedings 1 (19).
[24] N. Wiener, Generalized harmonic analysis, Acta Mathematica 55 (1) (1930) 117–258. doi:10.1007/BF02546511.
URL http://dx.doi.org/10.1007/BF02546511
[25] I. Langen, R. Sigbjörnsson, Dynamisk analyse av konstruksjoner: Dynamic analysis of structures, Tapir, 1979.
[26] H. Cramér, M. R. Leadbetter, Stationary and related stochastic processes: Sample function properties and their applications, Courier Corporation, 2013.
[27] B. Kinsman, Wind waves: their generation and propagation on the ocean surface, Courier Dover Publications, 1965.
[28] D. Hauser, K. Kahma, H. E. Krogstad, Measuring and analysing the directional spectra of ocean waves, Tech. rep. (2005).
[29] O. Faltinsen, Sea loads on ships and offshore structures, Vol. 1, Cambridge university press, 1993.
[30] T. Agar, Aerodynamic flutter analysis of suspension bridges by a modal technique, Engineering Structures 11 (2) (1989) 75–82. doi:10.1016/0141-0296(89)90016-3.
URL http://www.sciencedirect.com/science/article/pii/0141029689900163
[31] W. J. Pierson, L. Moskowitz, A proposed spectral form for fully developed wind seas based on the similarity theory of S. A. Kitaigorodskii, Journal of Geophysical Research 69 (24) (1964) 5181–5190. doi:10.1029/JZ069i024p05181.
URL http://dx.doi.org/10.1029/JZ069i024p05181
[32] K. Skogen, F. E. Dahl, Vind, strøm og bølger i Bergsøysundet (Krifast), Tech. rep., Veritas Offshore Technology and Services A/S (1989).
[33] M. S. Longuet-Higgins, D. E. Cartwright, N. D. Smith, Observations of the directional spectrum of sea waves using the motions of a floating buoy, in: Proc. Conf. Ocean Wave Spectra, Prentice-Hall, 1963, pp. 111–132.